FULL PAPER

Wearable Force Touch Sensor Array Using a Flexible and Transparent Electrode

Jun-Kyul Song, Donghee Son, Jaemin Kim, Young Jin Yoo, Gil Ju Lee, Liu Wang, Moon Kee Choi, Jiwoong Yang, Mincheol Lee, Kyungsik Do, Ja Hoon Koo, Nanshu Lu, Ji Hoon Kim, Taeghwan Hyeon, Young Min Song, and Dae-Hyeong Kim**

Transparent electrodes have been widely used for various electronics and optoelectronics, including flexible ones. Many nanomaterial-based electrodes, in particular 1D and 2D nanomaterials, have been proposed as next-generation transparent and flexible electrodes. However, their transparency, conductivity, large-area uniformity, and sometimes cost are not yet sufficient to replace indium tin oxide (ITO). Furthermore, the conventional ITO is quite rigid and susceptible to mechanical fractures under deformations (e.g., bending, folding). In this study, the authors report new advances in the design, fabrication, and integration of wearable and transparent force touch (touch and pressure) sensors by exploiting the previous efforts in stretchable electronics as well as novel ideas in the transparent and flexible electrode. The optical and mechanical experiment, along with simulation results, exhibit the excellent transparency, conductivity, uniformity, and flexibility of the proposed epoxy-copper-ITO (ECI) multilayer electrode. By using this multi-layered ECI electrode, the authors present a wearable and transparent force touch sensor array, which is multiplexed by Si nanomembrane p-i-n junction-type (PIN) diodes and integrated on the skin-mounted quantum dot light-emitting diodes. This novel integrated system is successfully applied as a wearable human–machine interface (HMI) to control a drone wirelessly. These advances in novel material structures and system-level integration strategies create new opportunities in wearable smart displays.

1. Introduction

Over the past few years, extensive research efforts have been devoted to develop new transparent and flexible electrodes[1–3] with reduced cost, large area uniformity, and excellent electrical, mechanical, and optical properties, to replace the indium tin oxide (ITO) as well as to apply to next-generation soft electronics/optoelectronic devices. An oxide/metal/oxide multilayer system,[4] for example, has been proposed to be a cheaper option with higher conductivity than ITO. However, its mechanical and optical properties are not good enough, particularly for flexible,[5,6] foldable,[7] and stretchable[8,9] electronics and optoelectronic devices. Many studies have alternatively focused on various nanomaterials,[10] such as carbon nanotubes,[11,12] graphene,[13–17] and silver (Ag) nanowire networks.[18–20] However, their physical properties such as surface uniformity, transparency, conductivity, and sometimes the cost, are not yet sufficient to replace ITO. The uniform integration of these

J.-K. Song, Dr. D. Son, J. Kim, Dr. M. K. Choi, Dr. J. Yang, M. Lee, K. Do, J. H. Koo, Prof. T. Hyeon, Prof. D.-H. Kim
Center for Nanoparticle Research
Institute for Basic Science (IBS)
Seoul 08826, Republic of Korea
E-mail: dkim98@snu.ac.kr

J.-K. Song, Dr. D. Son, J. Kim, Dr. M. K. Choi, Dr. J. Yang, M. Lee, K. Do, Prof. T. Hyeon, Prof. D.-H. Kim
School of Chemical and Biological Engineering
Institute of Chemical Processes
Seoul National University
Seoul 08826, Republic of Korea

Y. J. Yoo, G. J. Lee, Prof. Y. M. Song
School of Electronical Engineering and Computer Science
Gwangju Institute of Science and Technology
Gwangju 61005, Republic of Korea
E-mail: ymsong@gist.ac.kr

L. Wang, Prof. N. Lu
Center for Mechanics of Solids
Structures and Materials
Department of Aerospace Engineering
and Engineering Mechanics
Department of Biomedical Engineering
Texas Materials Institute
University of Texas at Austin
210 E. 24th Street, Austin, TX 78712, USA

J. H. Koo, Prof. D.-H. Kim
Interdisciplinary Program for Bioengineering
Seoul National University
Seoul 08826, Republic of Korea

Prof. J. H. Kim
School of Mechanical Engineering
Pusan National University
Busan 46269, Republic of Korea

DOI: 10.1002/adfm.201605286

nanomaterials with electronics, particularly for "gate/source/drain" electrode and vertical interconnect access (VIA) contact, also remains as a major challenge. Recent research using the coordination bonding between a self-assembled monolayer and Ag to develop an ultrathin Ag electrode[21] may be considered as an alternative electrode. However, several issues, such as low thermal reliability and incompatibility with through-dielectric VIA interconnection processes, still remain. Therefore, a novel electrode that satisfies all requirements, i.e., good mechanical deformability, high conductivity even in small patterns, optical transparency, uniformity over a large area, reasonable cost, and device fabrication compatibility, is highly needed.

We herein present a transparent and flexible electrode based on an epoxy-copper (Cu)-ITO (ECI) multilayer system. The ITO film with a minimum thickness is used to interconnect the electrodes through a VIA hole during the through-dielectric VIA interconnection process. An ultrathin low-cost copper film is deposited on the ITO film to improve the conductivity. A photocurable epoxy (SU8 2000.5, Microchem, USA) layer with a low refractive index is spin coated on the Cu film to enhance the optical transparency by virtue of a destructive interference.[22] The epoxy layer also dramatically increases the mechanical deformability of the ECI multilayer. The optical simulation theoretically proves that the transparency of the ECI multilayer is better than that of an ITO-Cu-ITO (ICI) multilayer.[23,24] Furthermore, the bending test and the mechanical analysis show that the epoxy layer successfully protects the Cu-ITO (CI) layer from the surface-stress-induced cracks under applied pressures. We then apply the ECI multilayer as a transparent and flexible interconnection of wearable force touch sensor array composed of touch[25] and pressure[26,27] sensors. Although there has been rapid progress in flexible pressure sensors[28] using piezoresistive,[29] triboelectric,[30] and piezo-photonic effects,[31,32] there are still huge needs for an integrated system of touch and pressure sensors for many wearable electronics applications. The force touch sensor array (10 × 10) is multiplexed by Si nanomembrane (SiNM) p-i-n junction (PIN) diodes.[33] The system transparency allows a clear view of the underlying co-integrated wearable quantum dot light-emitting diodes (QLEDs).[3,34] The uniform multilayer film maintains the high conductivity even after the interconnection patterning with narrow linewidths.[18] Moreover, we have successfully demonstrated that a drone can be controlled wirelessly using the wearable force touch sensor array. These material advances and system-level demonstrations using the ECI multilayer enable the wearable smart display[3,34,35] and novel human–machine interfaces (HMIs).[36–38]

2. Results and Discussion

2.1. Optical Characteristics of ECI in Comparison with CI and ICI

Figure 1a shows the schematic illustrations of the dependence of the calculated reflectance spectra on the optical thicknesses of each layer in CI, ICI, and ECI multilayer. The reflectance increases in the Cu layer; however, periodic reflectance changes are found in the top ITO layer in ICI and epoxy in ECI because of the interference of reflected waves at the surfaces and interfaces of each layer. The minimum dip of the ECI is remarkably lower than that of the ICI. Such a tendency can be analyzed using the admittance loci method (Figure 1b–e). The reflectance (R) in thin film optics can be expressed as $R = [(1 - Y)/(1 + Y)]^2$, where Y is the optical admittance defined by the ratio of the magnitudes of the magnetic to electric fields.[39] The zero reflection is basically obtained at the locus of the admittance reaching that of the air (1, 0). Starting from the end point of admittance in the bottom layer, the locus of the dielectric layer such as ITO and epoxy, repeatedly rotates in the clockwise direction with increasing film thickness. The epoxy plot more closely crosses the locus of the admittance of air than that of the ITO (Figure 1b). As metals have a non-trivial locus due to an imaginary part of refractive index, the end point of admittance reaches far away from that of the air with the increase in thickness (Figure 1c). The ECI further reduces the disparity with the admittance of air than the ICI (Figure 1d,e).

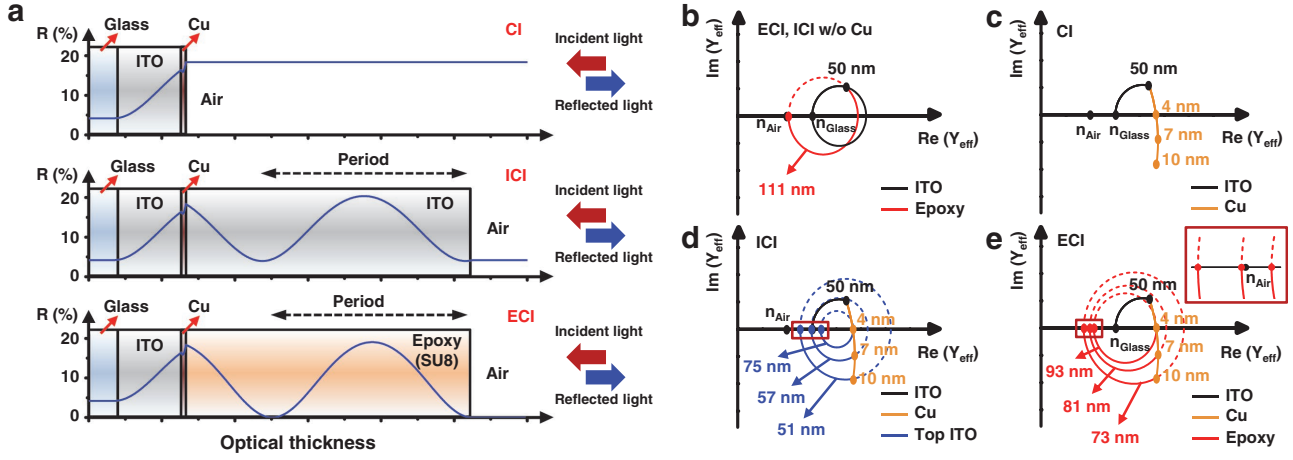

Figure 1. Optical characteristics of ECI in comparison with those of CI and ICI. a) Reflectance spectra of CI, ICI, and ECI as a function of optical thickness at a wavelength of 600 nm, with schematic illustrations. Admittance diagrams of the b) ECI and ICI without Cu, c) CI, d) ICI, and e) ECI at a wavelength of 600 nm.

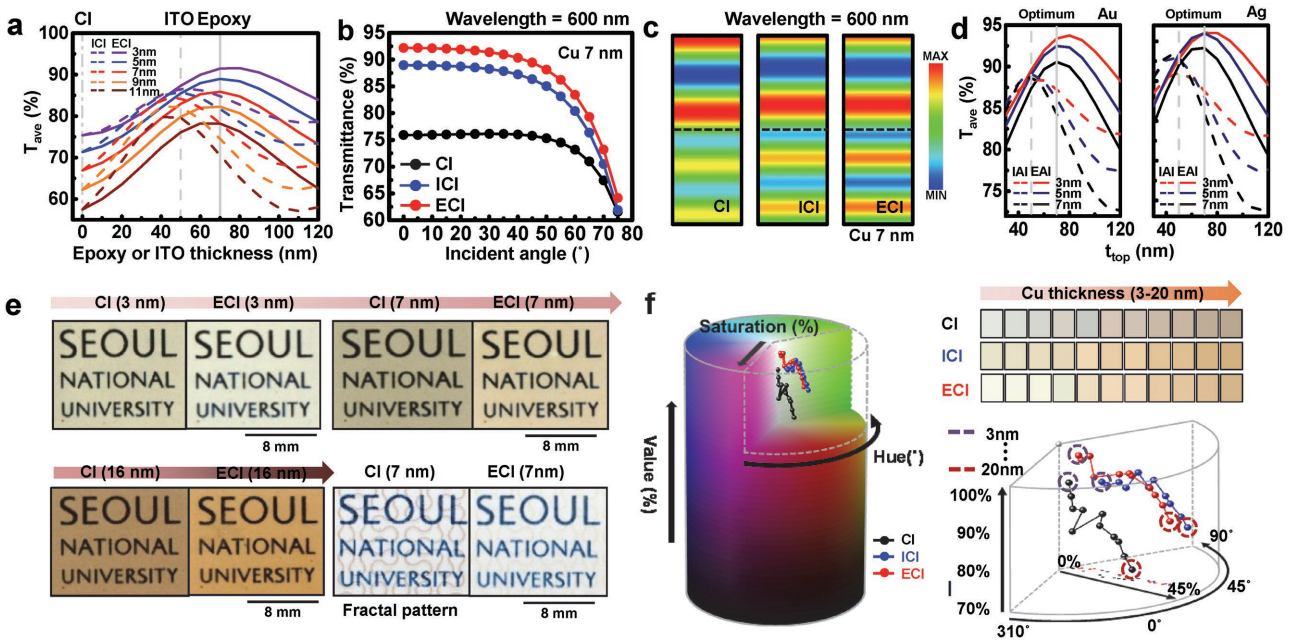

Figure 2. Optical characteristics of ECI in comparison with those of CI and ICI. a) Average transmittances of ICI and ECI in function of the thicknesses of Cu and the top layer (t_{top}) in the visible range. b) Dependency of transmittances on incident angles at a wavelength of 600 nm. c) Electrical field distributions of CI, ICI, and ECI at a wavelength of 600 nm. d) Transmission characteristics of the structures using other metals (e.g., Au and Ag). e) Images of CI and ECI with different thicknesses (e.g., 3, 7, and 16 nm). Fractal patterned with a thickness of 7 nm was also displayed. f) 3-D HSV (e.g., hue, saturation, and value) color map containing chromatic information of CI, ICI, and ECI (left) and its specific view using a cylindrical coordinate (bottom right). Color representations from the measured transmittances of CI, ICI, and ECI (top right).

The average transmittances were calculated based on the transmittance spectra of the ICI and ECI in the visible range for the different top layer thickness (t_{top}) with different Cu thickness (Figures S1 and S2, Supporting Information). Both t_{top} of ICI and ECI multilayers have a specific value enabling the highest average of transmittance in each of the different Cu thickness (**Figure 2**a). Therefore, we could choose the optimum t_{top} of ICI and ECI multilayers as 50 and 70 nm, respectively. The ECI at the optimum thickness with a Cu thickness of 7 nm ensures a higher transmittance than the other structures, regardless of the angle of incidence (Figure 2b). The ECI also shows electric field propagation with lower loss in intensity of field (Figure 2c). Covering epoxy on the other metals has been also considered to secure universality with other metals, such as Au and Ag. The result is analogous to the above mentioned tendency (Figure 2d). Other transparent polymers (i.e., polyimide (PI) and polymethyl methacrylate) instead of epoxy can be used, whose influence is shown in Figure S3 in the Supporting Information. Comparison about real images of the CI and ECI shows that the ECIs for all cases are more transparent than the CIs (Figure 2e). For quantitative comparison in terms of color, we reconstructed the transmittance measurement into a 3D hue, saturation, and value (HSV) color map of the CI, ICI, and ECI as depicted in Figure 2f (Table S1, Supporting Information). Being adjacent to the pure white point (0, 0, 100) in the HSV color map indicates that the samples (i.e., CI, ICI, and ECI) are more colorless. The ECI coordinate is closer to pure white than the CI and ICI (Figure 2f, bottom right). Reproduced colors from the HSV values are comparable to the real images of the CI and ECI in Figure 2e,f, (top right).

2.2. Mechanical Deformability of ECI in Comparison with Thick-ITO and ICI

In addition to the transparency, the high conductivity and mechanical deformability are key factors in flexible electronics and/or optoelectronics. An ultrathin ECI electrode with optimum epoxy-Cu-ITO thicknesses meets all of these requirements. We measured the sheet resistances of the Cu-ITO multilayers with a Cu thickness ranging from 3 to 20 nm (**Figure 3**a). The sheet resistance of the 7 nm Cu and 50 nm ITO bilayer is 50 Ω $\square^{-1}$, which is sufficient and in a good balance with the transparency (90% at 600 nm wavelength; including a glass substrate). ITO on a glass substrate, as a comparison, has 98% transparency at 600 nm wavelength. The Cu thickness can be tuned for higher conductivity (9 nm; 17 Ω $\square^{-1}$, 80% transparency at 600 nm wavelength) or higher transparency (5 nm; 78 Ω $\square^{-1}$, 92% transparency at 600 nm wavelength) depending on the application.

The stress-induced conductivity degradation can be indicated by the increase of electrical resistance at various bending radii. The ECI exhibited superb mechanical robustness in comparison with ICI and 200 nm thick ITO (Figure 3b). The 200 nm-thick ITO was used to match the resistance between the electrodes. Each structure was bent with different bending radii using a custom-made bending stage. The ECI maintained its high electrical conductivity even after the bending, whereas the ICI and thick ITO experienced an abrupt resistance increase. Furthermore, both ICI and thick ITO showed more significant resistance change ($\Delta R/R_0 = (R - R_0)/R_0$, where R and R_0 represent the final and initial resistance, respectively) under a cyclic bending test (Figure 3c).

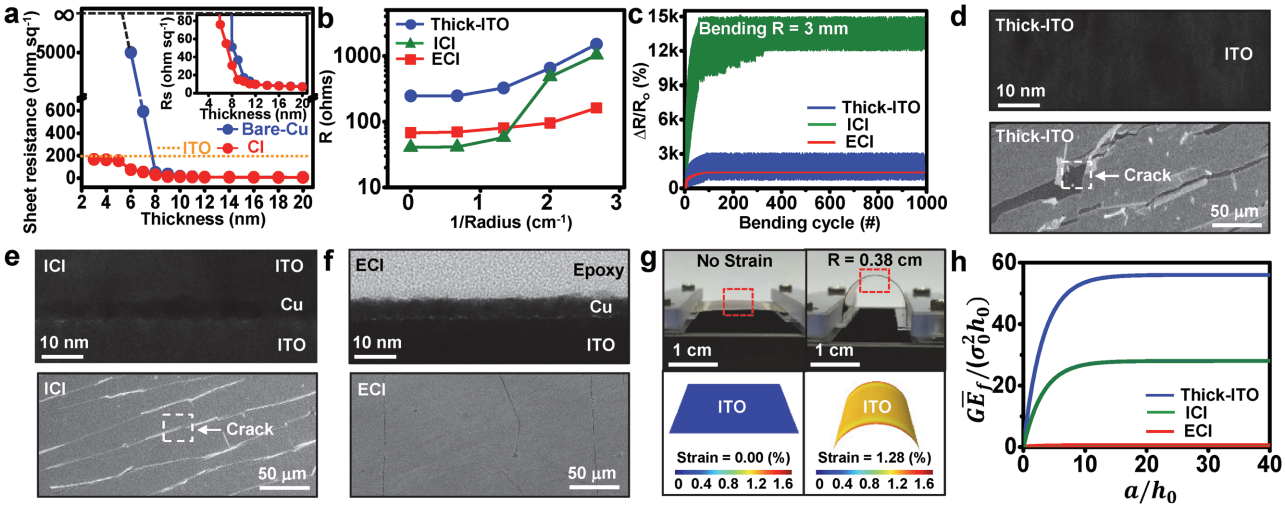

Figure 3. Mechanical characteristics of ECI in comparison with thick ITO and ICI. a) Sheet resistance of Cu-ITO (red) and Cu (blue), whose Cu thickness ranges from 3 to 20 nm. The orange dotted line shows the sheet resistance of the 100 nm-thick ITO. b) Change in the resistance per unit length of ECI, thick ITO, and ICI at various bending radii. c) Durability test of ECI, thick ITO, and ICI by repetitive bending. d-f) Cross-sectional TEM images (top) before bending and the SEM images of the ITO surface after bending (bottom) for d) thick ITO, e) top ITO layer of ICI, f) bottom ITO layer of ECI. g) FEA results showing the strain distribution of the ITO layer at different bending conditions under bending at $R = \infty$ and 0.38 cm (bottom) and corresponding images of bent sample (top). h) Plot of the normalized energy release rates versus the crack length of thick ITO, ICI, and ECI (G = the energy release rate of channel cracking, $\bar{E}_f$ = the plane strain modulus of the film, σ_0 = the stress in the film, h_0 = 50 nm).

Figure 3d–f upper frames display the cross-sectional transmission electron microscopy (TEM) images of thick ITO, ICI, and ECI to reveal the structural information of each. The corresponding cross-sectional schematics and thickness information are offered in Figure S5a–c in the Supporting Information. The corresponding top-view scanning electron microscope (SEM) images in the lower frames of Figure 3d,e confirm that the large difference of resistance change in thick ITO and ICI (Figure 3b) is caused by the mechanical fracture of the topmost ITO. In case of the ECI, we etched the topmost epoxy and Cu layers after bending of the ECI, and verified the morphology changes in the bottom ITO surface (Figure 3f, bottom). Only minimal cracks were observed showing the meaningful role of the epoxy layer in preventing mechanical failures.

More in-depth investigations on the bending-induced electrode degradation were performed using the finite element analysis (FEA) and thin film mechanical theories. The strain distribution in the ITO layer of the ECI structure modeled by FEA (Figure 3g) is consistent with the analytical predictions summarized in Table S2 in the Supporting Information. Both FEA and analytical results indicate that there is almost no difference in ITO strain across the three different structures when subjected to the same bending radius. This finding is attributed to the large thickness of the PI layer (100 μm) compared with the functional layers on the top. However, among the three investigated structures, the ECI structure exhibits a minimal increment of resistance, which indicates the least fracture in the ITO of the ECI even if it experiences similar strains as the ITO in the other two structures. This result has to be obtained through the analysis of the energy release rate (i.e., the elastic energy reduced upon crack propagates unit area), which should be a more rigorous fracture indicator than the often used tensile strain in the material.

Griffith's fracture criterion suggests that a crack will propagate when the energy release rate exceeds the intrinsic toughness of the material. Therefore, we calculated the energy release rate in the ITO layer of the three different structures. On one hand, the channel cracks, as illustrated in Figure S6a in the Supporting Information, are formed in the top ITO layer of the thick ITO and ICI structures. On the other hand, the tunnel cracks, as illustrated in Figure S6b in the Supporting Information, are formed in the ECI ITO layer, which is sandwiched between polymers (the 7 nm thick Cu is neglected). The energy release rates for the channel and tunnel cracks are both dependent on the crack length when the crack is short, but it will eventually reach a steady state when the cracks are long enough. Figure 3h represents the relation between energy release rates with the crack length, and the analytical calculation of the energy release rates are shown in the Supporting Information. As expected, the tunnel cracks in the ECI ITO layer have a much lower steady state energy release rate compared with the channel cracks in the top ITO layer of the thick ITO and ICI structures. Since the intrinsic toughness of the ITO is a constant, the ITO layer with a lower energy release rate is less prone to crack propagation. This result implies that the ECI structure is less likely to undergo ITO fracture compared with the other two structures. Comparing the thick ITO with the ICI, the ICI ITO has a lower steady-state energy release rate, which explains the lower resistance increment of the ICI than the thick ITO (Figure 3b). In summary, the energy release rate is more reliable for fracture criterion in the ruptured films by different cracks (i.e., channel cracks vs tunnel cracks) compared with the tensile strain in the material.

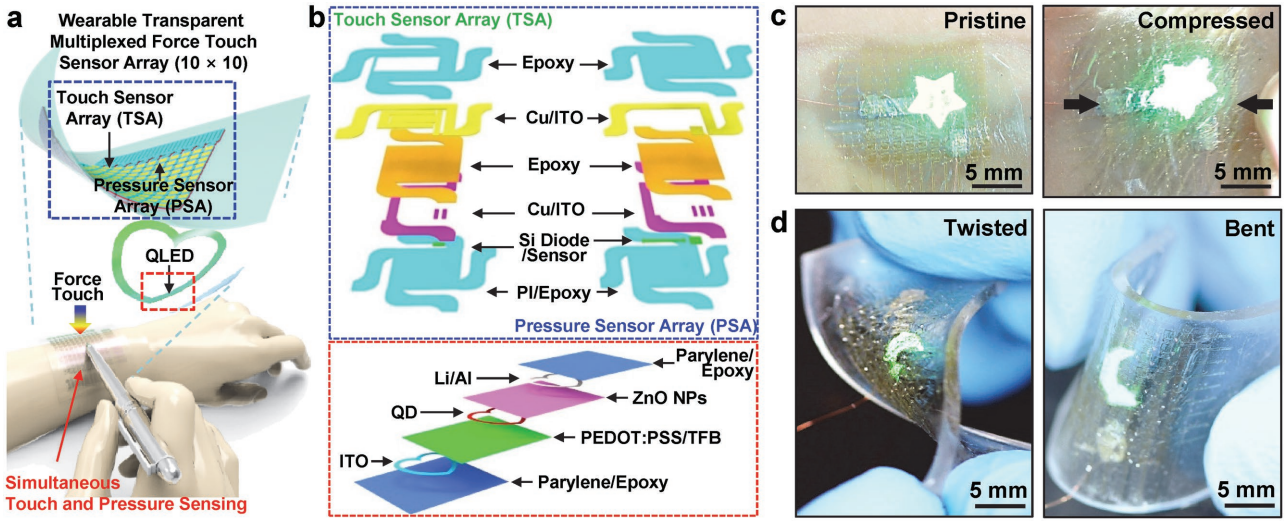

Figure 4. Transparent and wearable force touch sensor array. a) Schematic illustration of the wearable multiplexed force touch sensor array integrated with the skin-mounted QLED. b) Exploded view of the multiplexed force touch sensor array comprising six stacked layers (top) and of the QLED comprising seven layers (bottom). c) Images of the transparent and ultrathin device on skin-mounted QLEDs conformally laminated on human wrist (left) and its compressed form (right). d) Deformed wearable devices on the ultrathin QLEDs by twisting (left) and bending (right).

2.3. Electrical Characterization of the Wearable Force Touch Sensor Array

We fabricate the transparent multiplexed force touch sensor array by using the ECI electrode on wearable QLEDs (**Figure 4**a). The system is composed of wearable touch and pressure sensors, which are multiplexed by SiNM PIN diodes and embedded wearable QLEDs (magnified view of the stacked layers is presented in Figure 4b). The system can be conformally integrated on the pristine and compressed human skin (Figure 4c). The device transferred to an ≈2 mm-thick handle polydimethylsiloxane (PDMS) sheet shows no mechanical fractures under twisting and bending deformations (Figure 4d). The mechanical softness of the device enables its conformal integration on the deformed human skin only with the van der Waals force.[40,41] The detailed fabrication procedures are described in the experimental section.

Figure 5a,b show an optical image and a corresponding circuit diagram of the multiplexed force touch sensor array (10 × 10), respectively. The single cell images of touch and pressure sensors are shown in Figure 5a inset. The device shown in Figure 5a was fabricated using Cr/Au electrode in order to clearly indicate the electrodes, while the transparent version is shown in Figures 4c and 5h. The operation sequence of the sensor array is as follows: touch information is acquired when a conductive fabric is in contact to the interdigitated touch sensor array. At the same time, pressure information can be monitored by the SiNM-based pressure sensor, whose sensitivity is enhanced by modulating the neutral mechanical plane to the off-center position through adoption of a cavity-induced asymmetrical structure[29] (detailed schematic illustration in Figure S7, Supporting Information). The touch/pressure information can be reliably multiplexed by highly conductive serpentine interconnects,[42] even under applied pressures.

The 35 PIN diodes show uniform electrical performances (Figure 5c), which are suitable for multiplexing the sensor signals. In addition to the high quality single crystal silicon electronics,[43] the highly conductive ECI electrodes enable the sensor array to have high uniformity. The high conductivity of the ECI electrodes minimized the differences of the operation voltage/current between the near and far cells in the array, while ITO electrodes exhibit larger differences (Figure 5d).

We first characterized the single touch sensor in touch sensor array that is in contact with a conductive fabric on a fingertip (Figure S8, Supporting Information). There are clear differences between the amplitudes of the current when the touch sensor is in contact with a conductive fabric, a finger, or nothing (Figure S9, Supporting Information). Figure 5e shows the voltage map data of the touch sensor array in contact with a conducting object. A custom-made software was used to monitor the touched area in real-time (Movie S1, Supporting Information). We also measured pressure information from a single pressure sensor in the force touch sensor array. Figure 5f shows a calibration curve of the pressure sensor. The sensor starts to react after certain amount of pressure (≈40 kPa) due to the viscoelastic substrate underneath the force touch sensor array. When the pressure larger than 40 kPa is applied, the sensor's output voltage difference increases linearly. The inset shows the output voltage change of the pressure sensor when different pressures are successively applied. Additionally, the pressure sensor can dynamically measure varying pressures (Figure 5g). In contrast to the touch sensors, the pressure sensor exhibits marginal delays (0.36–0.22 ms = 0.14 ms) of the response time due to viscoelastic properties of the polymeric substrate underneath the pressure sensor (inset). The wearable force touch sensor array can be conformably integrated with the ultrathin QLEDs (Figure 5h), which show outstanding device performances, such as a high brightness up to 20,000 cd m^{-2}

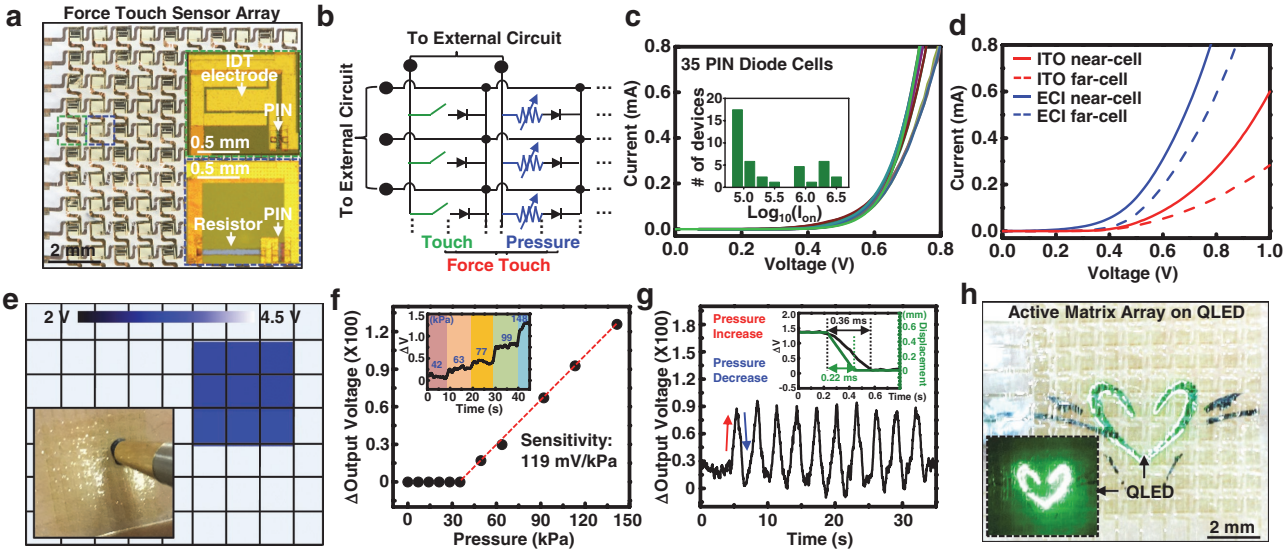

Figure 5. Electrical characteristics of the multiplexed force touch sensor array consisting of touch and pressure sensors. a) Optical image of the multiplexed force touch sensor array (10 × 10) intentionally fabricated with metal electrode to clearly show its appearance. The insets show magnified images of a single cell, which consists of the interdigitated pattern of the touch sensor (top) and the pressure sensor (bottom). b) Circuit schematic of the multiplexed array to address individual sensor. c) Representative current-voltage (*I*–*V*) curves of 35 PIN diodes. The inset shows the on-current distribution at 1 V. d) Comparison of the *I*–*V* curves of PIN diodes using the Cu-ITO and ITO-based electrodes between the near and far cells. e) Voltage map measured from the touch sensor array in contact with a conductive material. f) Calibration curve of the pressure sensor with various applied pressures. The inset shows the real-time response (filtered by 3 Hz low-pass filter) of the pressure sensor according to the applied pressure changes. g) Output voltage change of the pressure sensor with varying amounts of applied pressure (from 0 to 113 kPa). The inset shows the displacement (green) of the pressure sensor when the pressure (198 to 35 kPa) is applied by a cylindrical tip and the corresponding output voltage change (black) of the pressure sensor to show its response time. h) Multiplexed force touch sensor array integrated with the QLED. The entire integrated system is conformally laminated on the human skin. Inset shows the turned-on QLEDs under the dark condition.

at 9 V (Figure S10, Supporting Information) and the lifetime of 12,815 hours at 100 cd m^{-2} referred to in our previous report.[34] The transparency of the force touch sensor array allows for a clear view of the QLEDs underneath the sensors (Figure 5h; the inset shows a dark condition). This integrated system exhibits a significant potential for next-generation wearable electronic and optoelectronic devices.

2.4. HMI Based on the Force Touch Sensor Array for the Wireless Drone Control

A wearable HMI is demonstrated based on the force touch sensor array to wirelessly control a quadricopter drone (AR. Drone 2.0, Parrot SA, France). **Figure 6**a shows a schematic diagram of the data acquisition setup for the measurement of the touch and applied pressure by using the 10 × 10 force touch sensor array. Here, a load resistor (R_L) converts the electrical current modulated by the force touch sensor into electrical voltage, which is recorded by the data acquisition (DAQ) board (NI PXI-6289, USB-6003, National Instruments, USA). Figure 6b illustrates the output voltage change of the force touch sensors according to the touch and the applied pressure. The output voltage of the touch sensor (black) remains at V_{CC} of 5 V when the touch sensor is not in contact. The output voltage is then abruptly decreased once the conductive material contacts the touch sensor because R_L and the force touch sensor form a voltage divider circuit. Then, the simultaneously measured output voltage signal of the pressure sensor (blue) also changes according to the applied pressure. The force touch sensor can detect the pressure variations while the sensor array is in contact with a conductive fabric (Figure S11, Supporting Information). Figure 6c depicts the output voltage changes of the touch sensors when the conductive fabric attached on a fingertip is in contact with the corresponding sensors (T1–T4) individually (single touch) or together (multi-touch). No cross-talks between the adjacent touch sensors were observed.

Figure 6d illustrates the role of touch sensors (T1–T4) and pressure sensors (P1–P2) during the wireless control of drone. Here, the drone takes off or lands when all touch sensors (T1–T4) detect the touch. The touch of an individual touch sensor (T1, T2, T3, and T4) moves the drone to the forward, left, backward, and right directions, respectively. In addition, applying pressures on the individual pressure sensor (P1–P2) moves the drone to upward and downward directions, respectively. A custom-made code written by using LabVIEW (National Instruments, USA) was used to record the signals and transmit the commands (Figure S12, Supporting Information). Figure 6e illustrates the algorithm of the drone control. First, the software checks the number of sensors touched. When all four sensors are touched, the software sends a command to the drone to take off. After the drone takes off, the software individually analyzes the contact status of each sensor to control the drone's moving direction. Lastly, the drone lands on the ground when all sensors are touched together again. The classifier accuracy is illustrated by a confusion matrix, in which the column and row represent the predicted class and the actual class, respectively (Figure S13, Supporting Information). The success rate of

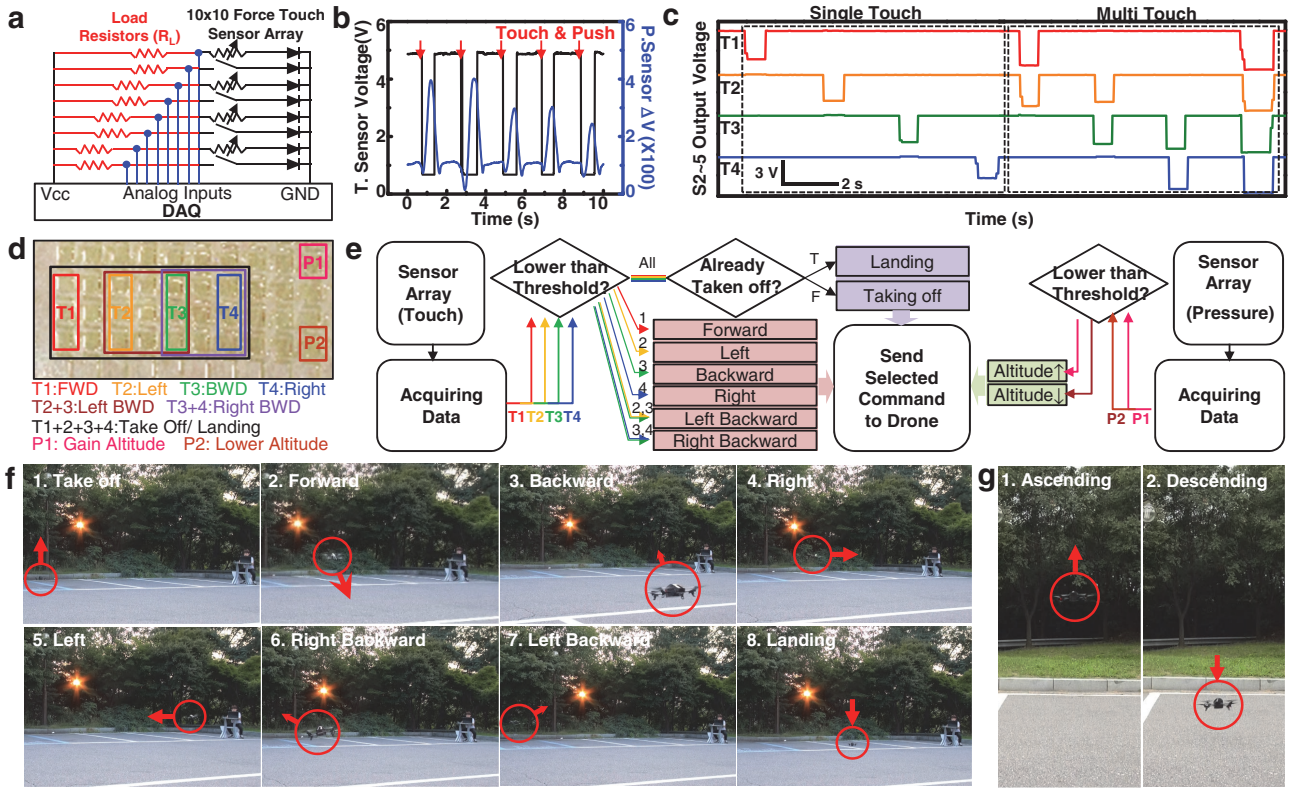

Figure 6. Wireless drone control demonstration using the wearable force touch sensor array. a) Schematic illustration of the measurement and data acquisition setup. b) Output voltage change of the force touch sensor when the conductive material touches and applies pressure to the sensor (T. sensor: touch sensor, P. sensor: pressure sensor). c) Output voltage changes of the touch sensors (T1–T4) when the individual sensor is touched and/or multiple sensors are touched. d) Optical image of the force touch sensor array showing the role of the sensors in drone control (FWD: forward, BWD: backward). e) Flow chart showing the algorithm of the drone control software. f) Images of the wireless drone control using the touch sensors and g) pressure sensors.

commands reaches almost 100% for 50 trials. For the altitude control, the software individually analyzes the signal changes of the pressure sensors. When P1 or P2 is pressed, the software sends a command to the drone to increase or decrease the altitude, respectively. As demonstrated in Figure 6f,g (Movie S2, Supporting Information), the drone can be successfully controlled by using the wearable force touch sensor array.

3. Conclusion

A new ECI electrode that exhibits the high optical transparency, electrical conductivity, and mechanical deformability is developed. Its superb optical, electrical, and mechanical properties are verified by a series of experiments and theoretical analyses. A wearable and transparent multiplexed force touch sensor array is developed by using the ECI electrode and integrated on the skin-mounted QLEDs. In addition to the transparency and flexibility of the ECI electrode, the large area uniformity and the processing compatibility with the sensor array fabrication enable the wearable human–machine interface for wireless drone control. The ECI electrode creates many new opportunities in the field of transparent electronics and wearable smart displays.

4. Experimental Section

Optical Calculation: The optical absorption spectra were obtained using a Cary 5000E UV–Vis–NIR spectrophotometer. A commercial software (The Essential Macleod, Thin Film Center, Inc., USA) based on the characteristic matrix method, involving multilayer structures, was employed to calculate the optical admittance for finding the layer-matching condition. The rigorous coupled-wave analysis (RCWA) was also used to calculate the CI, ICI, and ECI transmittance by using commercial software (DiffractMOD, RSoft Design Group, USA). The third diffraction order and 0.5 nm grid size were used in the RCWA to calculate the diffraction efficiency, which was sufficient to numerically stabilize the results. The non-polarized light transmittance was calculated by averaging the transmittances for the p and s linear polarizations. The optical constants of the ITO were measured by spectroscopic ellipsometry. The refractive index values for Cu and epoxy were taken from the literature and Microchem datasheets, respectively.[44,45] Material dispersion and extinction coefficient were considered in obtaining the exact outputs.

Fabrication of Force Touch Sensor Array: The fabrication was begun by defining the n- and p-doped regions on a silicon on insulator (340 nm Si on buried oxide) wafer with spin-on dopant at high temperature (≈975 °C) for the phosphorous and boron diffusion. The PIN diodes[33] were formed by using the patterned doped SiNM with the channel width and length of 200 and 10 µm, respectively. A PI precursor solution (polyamic acid, Sigma Aldrich, USA) was spin coated at 8000 rpm for 60 s on a SiO_2/Si substrate (4science, Korea) and annealed at 250 °C for 1 h, followed by epoxy resist spin coating (SU8 2, Microchem, USA) at

3000 rpm for 30 s. The doped SiNMs were then transfer printed on to the prepared substrate.[43] The PIN diodes were defined using reactive-ion etching (SF_6 plasma, 50 sccm flow rate, 40 mTorr chamber pressure, and 100 W RF power for 1 min) with photolithography. The sputtering and thermal evaporation for metallization (ITO/Cu, 50 nm/7 nm), photolithography, and wet-etching steps defined the serpentine metal lines followed by the spin coating of a diluted epoxy resist (SU8 2000.5, Microchem, USA) on the substrate. The epoxy pattern was defined through photolithography. The whole device was picked up and transferred to the PDMS (40:1 mixture of prepolymer:curing agent; Sylgard 184, Dow Corning, USA) spin coated on the polyvinyl alcohol film using a piece of thermal-release tape (TW-50R150, Tape World, Republic of Korea).[42] The electrical measurements were finally performed using a parameter analyzer (B1500A, Agilent, USA) and DAQ board.

Fabrication of QLED: An ITO glass substrate was sequentially washed with detergent, distilled water, and isopropanol. The substrate was then subjected to UV/O_3 treatment for 20 min. A 25 nm thick poly(3,4-ethylenedioxythiophene) polystyrene sulfonate (PEDOT:PSS) layer and a 20 nm thick poly[(9,9-dioctylfluorenyl-2,7-diyl)-co-(4,4′-(*N*-(4-sec-butylphenyl)diphenylamine)] (TFB) layer as a hole-transport layer were spin coated and annealed at 180 °C for 30 min. A 35 nm-thick quantum dot layer and a 45 nm thick ZnO nanocrystal layer were spin coated and annealed at 180 °C for 30 min in an Ar atmosphere. The CdSe quantum dots and the ZnO nanocrystals were synthesized according to the previously reported method.[34] A 50 nm thick Li-Al electrode was deposited as the cathode by thermal evaporation under a high vacuum.

Characterization of the Force Touch Sensor: The force touch sensor array or the touch sensor array was connected to the external circuit as shown in Figure 6a. The load resistors (R_L) were selected as 200 kΩ resistors, considering the effective resistance of a PIN diode. The custom-made software written with LabVIEW controlled various digital output terminals of the DAQ board to have appropriate potential so that the only one sensor in the multiplexed array could be addressed at a time. Once the certain potential was applied to a single sensor, the output voltage decided by ratio of R_L and the resistance of the sensor was transmitted to the analog input port of the DAQ to be measured. The changes of output voltage by the pressure sensor according to the change of the applied pressure was small (≈100 mV) due to the large resistance of multiplexing PIN diode and load resistors. In that sense, the output signal of the pressure sensor was filtered and amplified (100 times). To accurately calculate the applied pressure, a force gauge (M2-10, Mark-10, USA) was used with a cylindrical tip whose cross-sectional area was 7.07×10^{-6} m^2.

Supporting Information

Supporting Information is available from the Wiley Online Library or from the author.

Acknowledgements

J.-K.S., D.S., and J.K. contributed equally to this work. The work presented in this paper was supported by SAMSUNG DISPLAY Co., Ltd. This work was also supported by IBS-R006-D1 and by the Basic Science Research Program of the NRF funded by the MSIP (2014R1A1A1005945). N.L. acknowledges the US NSF CMMI award under Grant No. 1351875.

Received: October 11, 2016
Revised: November 8, 2016
Published online: December 28, 2016

[1] K. Ellmer, *Nat. Photonics* **2012**, *6*, 809.
[2] H. Wu, D. Kong, Z. Ruan, P.-C. Hsu, S. Wang, Z. Yu, T. J. Carney, L. Hu, S. Fan, Y. Cui, *Nat. Nanotechnol.* **2013**, *8*, 421.
[3] M. K. Choi, I. Park, D. C. Kim, E. Joh, O. K. Park, J. Kim, M. Kim, C. Choi, J. Yang, K. W. Cho, J.-H. Hwang, J.-M. Nam, T. Hyeon, J. H. Kim, D.-H. Kim, *Adv. Funct. Mater.* **2015**, *25*, 7109.
[4] D. Kim, *Trans. Electr. Electron. Mater.* **2009**, *10*, 165.
[5] M. Kaltenbrunner, T. Sekitani, J. Reeder, T. Yokota, K. Kuribara, T. Tokuhara, M. Drack, R. Schwodiauer, I. Graz, S. Bauer-Gogonea, S. Bauer, T. Someya, *Nature* **2013**, *99*, 458.
[6] Z. Bao, X. Chen, *Adv. Mater.* **2016**, *28*, 4177.
[7] D.-H. Kim, J.-H. Ahn, W.-M. Choi, H.-S. Kim, T.-H. Kim, J. Song, Y. Y. Huang, L. Zhuangjian, L. Chun, J. A. Roger, *Science* **2008**, *320*, 507.
[8] T. Someya, Y. Kato, T. Sekitani, S. Iba, Y. Noguchi, Y. Murase, H. Kawaguchi, T. Skurai, *Proc. Natl. Acad. Sci. USA* **2005**, *102*, 12321.
[9] S. Choi, H. Lee, R. Ghaffari, T. Hyeon, D.-H. Kim, *Adv. Mater.* **2016**, *28*, 4203.
[10] J. Yang, M. K. Choi, D.-H. Kim, T. Hyeon, *Adv. Mater.* **2016**, *28*, 1176.
[11] D. J. Lipomi, M. Vosgueritchian, B. C.-K. Tee, S. L. Hellstrom, J. A. Lee, C. H. Fox, Z. Bao, *Nat. Nanotechnol.* **2011**, *6*, 788.
[12] S. Bai, C. Sun, H. Yan, X. Sun, H. Zhang, L. Luo, X. Lei, P. Wan, X. Chen, *Small* **2015**, *43*, 5807.
[13] S. Bae, H. Kim, Y. Lee, X. Xu, J.-S. Park, Y. Zheng, J. Balakrishnan, T. Lei, H. R. Kim, Y. I. Song, Y.-J. Kim, K. S. Kim, B. Ozyilmaz, J.-H. Ahn, B. H. Hong, S. Iijima, *Nat. Nanotechnol.* **2010**, *5*, 574.
[14] H. Lee, T. K. Choi, Y. B. Lee, H. R. Cho, R. Ghaffari, L. Wang, H. J. Choi, T. D. Chung, N. Lu, T. Hyeon, S. H. Choi, D.-H. Kim, *Nat. Nanotechnol.* **2016**, *11*, 566.
[15] H. Lee, Y. Lee, C. Song, H. R. Cho, R. Ghaffari, T. K. Choi, K. H. Kim, Y. B. Lee, D. Ling, H. Lee, S. J. Yu, S. H. Choi, T. Hyeon, D.-H. Kim, *Nat. Commun.* **2015**, *6*, 10059.
[16] H. Jang, Y. J. Park, X. Chen, T. Das, M.-S. Kim, J.-H. Ahn, *Adv. Mater.* **2016**, *28*, 4184.
[17] S. J. Kim, K. W. Cho, H. R. Cho, L. Wang, S. Y. Park, S. E. Lee, T. Hyeon, N. Lu, S. H. Choi, D.-H. Kim, *Adv. Funct. Mater.* **2016**, *26*, 3207.
[18] M.-S. Lee, K. Lee, S. Y. Kim, H. Lee, J. Park, K.-H. Choi, H.-K. Kim, D.-G. Kim, D.-Y. Lee, S. Nam, J.-U. Park, *Nano Lett.* **2013**, *13*, 2814.
[19] D. S. Hecht, L. B. Hu, G. Irvin, *Adv. Mater.* **2011**, *23*, 1482.
[20] B.-U. Hwang, J.-H. Lee, T. Q. Trung, E. Roh, D.-I. Kim, S.-W. Kim, N.-E. Lee, *ACS Nano* **2016**, *9*, 8801.
[21] H. Kang, S. Jung, S. Jeong, G. Kim, K. Lee, *Nat. Commun.* **2015**, *6*, 6503.
[22] G. H. Jung, K. Hong, W. J. Dong, S. Kim, J.-L. Lee, *Adv. Energy Mater.* **2011**, *1*, 1023.
[23] S. Kim, H. W. Cho, K. Hong, J. H. Son, K. Kim, B. Koo, S. Kim, J.-L. Lee, *Opt. Express* **2014**, *22*, A1257.
[24] C. Guillén, J. Herrero, *Sol. Energy Mater. Sol. Cells* **2008**, *92*, 938.
[25] B. Zhu, Z. Niu, H. Wang, W. R. Leow, H. Wang, Y. Li, L. Zheng, J. Wei, F. Huo, X. Chen, *Small* **2014**, *18*, 3625.
[26] C. Yeom, K. Chen, D. Kiriya, Z. Yu, G. Cho, A. Javey, *Adv. Mater.* **2015**, *27*, 1561.
[27] L. Pan, A. Chortos, G. Yu, Y. Wang, S. Isaacson, R. Allen, Y. Shi, R. Dauskardt, Z. Bao, *Nat. Commun.* **2014**, *5*, 3002.
[28] X. Wang, L. Dong, H. Zhang, R. Yu, C. Pan, Z. L. Wang, *Adv. Sci.* **2015**, *2*, 1500169.
[29] J. Kim, M. Lee, H. J. Shim, R. Ghaffari, H. R. Cho, D. Son, Y. H. Jung, M. Soh, C. Choi, S. Jung, K. Chu, D. Jeon, S.-T. Lee, J. H. Kim, S. H. Choi, T. Hyeon, D.-H. Kim, *Nat. Commun.* **2014**, *5*, 5747.
[30] X. Wang, H. Zhang, L. Dong, X. Han, W. Du, J. Zhai, C. Pan, Z. L. Wang, *Adv. Mater.* **2016**, *28*, 2896.
[31] C. Pan, L. Dong, G. Zhu, S. Niu, R. Yu, Q. Yang, Y. Liu, Z. L. Wang, *Nat. Photonics* **2013**, *7*, 752.
[32] X. Wang, H. Zhang, R. Yu, L. Dong, D. Peng, A. Zhang, Y. Zhang, H. Liu, C. Pan, Z. L. Wang, *Adv. Mater.* **2015**, *27*, 2324.

[33] R. C. Webb, A. P. Bonifas, A. Behnaz, Y. Zhang, K. J. Yu, H. Cheng, M. Shi, Z. Bian, Z. Liu, Y.-S. Kim, W.-H. Yeo, J. S. Park, J. Song, Y. Li, Y. Huang, A. M. Gorbach, J. A. Rogers, *Nat. Mater.* **2013**, *12*, 938.
[34] M. K. Choi, J. Yang, K. Kang, D. C. Kim, C. Choi, C. Park, S. J. Kim, S. I. Chae, T.-H. Kim, J. H. Kim, T. Hyeon, D.-H. Kim, *Nat. Commun.* **2015**, *6*, 7149.
[35] T. Yokota, P. Zalar, M. Kaltenbrunner, H. Jinno, N. Matsuhisa, H. Kitanosako, Y. Tachibana, W. Yukita, M. Koizumi, T. Someya, *Sci. Adv.* **2016**, *2*, e1501856.
[36] S. Lim, D. Son, J. Kim, Y. B. Lee, J.-K. Song, S. Choi, D. J. Lee, J. H. Kim, M. Lee, T. Hyeon, D.-H. Kim, *Adv. Funct. Mater.* **2015**, *25*, 375.
[37] S. Jung, J. H. Kim, J. Kim, S. Choi, J. Lee, I. Park, T. Hyeon, D.-H. Kim, *Adv. Mater.* **2014**, *26*, 4825.
[38] T. Q. Trung, N.-E. Lee, *Adv. Mater.* **2016**, *28*, 4338.
[39] H. A. Macleod, *Thin-Film Optical Filters*, 2nd ed., Macmillan, New York **1986**.
[40] M. K. Choi, O. K. Park, C. Choi, S. Qiao, R. Ghaffari, J. Kim, D. J. Lee, M. Kim, W. Hyun, S. J. Kim, H. J. Hwang, S.-H. Kwon, T. Hyeon, N. Lu, D.-H. Kim, *Adv. Healthcare Mater.* **2016**, *5*, 80.
[41] D. Son, J. H. Koo, J.-K. Song, J. Kim, M. Lee, H. J. Shim, M. Park, M. Lee, J. H. Kim, D.-H. Kim, *ACS Nano* **2015**, *9*, 5585.
[42] D. Son, J. Lee, S. Qiao, R. Ghaffari, J. Kim, J. E. Lee, C. Song, S. J. Kim, D. J. Lee, S. W. Jun, S. Yang, M. Park, J. Shin, K. Do, M. Lee, K. Kang, C. S. Hwang, N. Lu, T. Hyeon, D.-H. Kim, *Nat. Nanotechnol.* **2014**, *9*, 397.
[43] J. Kim, D. Son, M. Lee, C. Song, J.-K. Song, J. H. Koo, D. J. Lee, J. Shim, J. H. Kim, M. Lee, T. Hyeon, D.-H. Kim, *Sci. Adv.* **2016**, *2*, E1501101.
[44] H.-J. Hagemann, W. Gudat, C. Kunz, *J. Opt. Soc. Am.* **1975**, *65*, 742.
[45] MicroChem, SU-8 Data Sheet, http://www.microchem.com/pdf/SU-82000DataSheet2000_5thru2015Ver4.pdf (accessed: July 2016).

ADVANCED FUNCTIONAL MATERIALS

Supporting Information

for *Adv. Funct. Mater.*, DOI: 10.1002/adfm.201605286

Wearable Force Touch Sensor Array Using a Flexible and Transparent Electrode

Jun-Kyul Song, Donghee Son, Jaemin Kim, Young Jin Yoo, Gil Ju Lee, Liu Wang, Moon Kee Choi, Jiwoong Yang, Mincheol Lee, Kyungsik Do, Ja Hoon Koo, Nanshu Lu, Ji Hoon Kim, Taeghwan Hyeon, Young Min Song, and Dae-Hyeong Kim**

Supporting Information

Wearable force touch sensor array using a flexible and transparent electrode

Jun-Kyul Song†, Donghee Son†, Jaemin Kim†, Young Jin Yoo, Gil Ju Lee, Liu Wang, Moon Kee Choi, Jiwoong Yang, Mincheol Lee, Kyungsik Do, Ja Hoon Koo, Nanshu Lu, Ji Hoon Kim, Taeghwan Hyeon, Young Min Song, Dae-Hyeong Kim**

Supporting Information 1: Transmittance spectra of ICI and ECI.

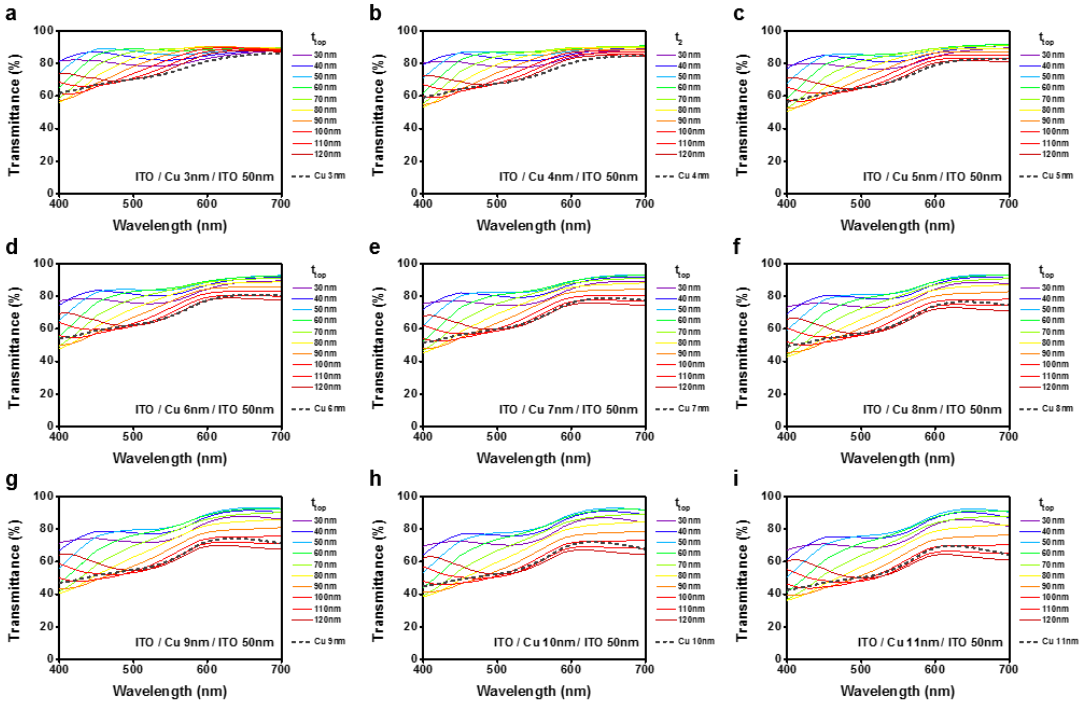

Figure S1. Calculated transmittance spectra with various top layer thicknesses (t_{top}) variations (*i.e.*, 30-120 nm) of ICI with different Cu thickness (*i.e.*, 3-11 nm).

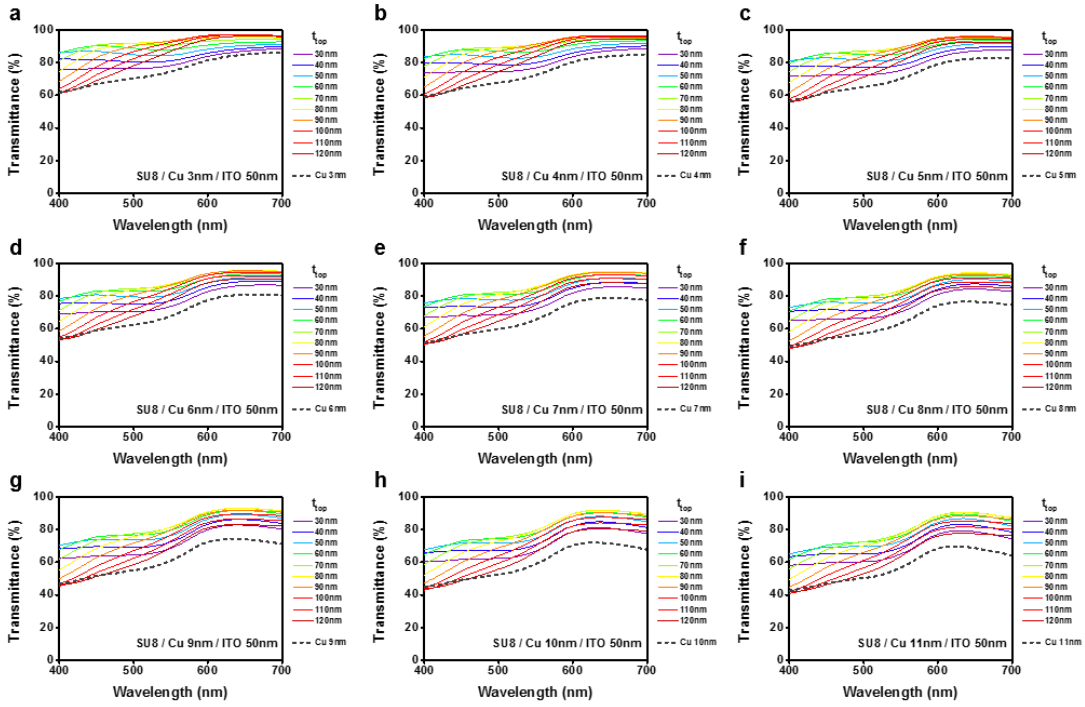

Figure S2. Calculated transmittance spectra with various top layer thicknesses (t_{top}) variations (*i.e.*, 30-120 nm) of ECI with different Cu thickness (*i.e.*, 3-11 nm).

Supporting Information 2: Other transparent polymers.

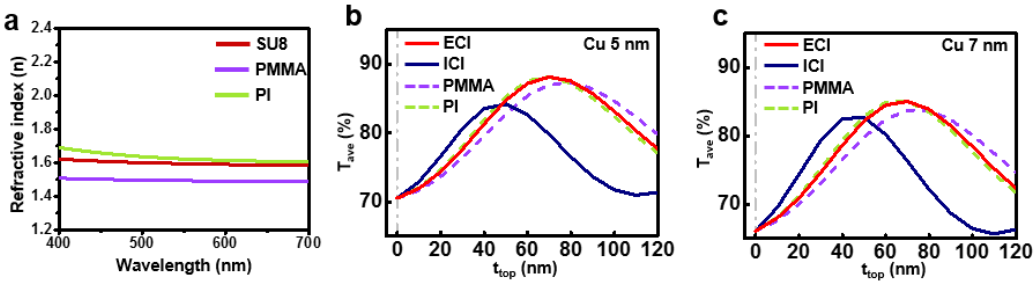

Figure S3. a) Refractive indices of transparent polymers. b) Transmittance compared with that of ECI and ICI when other transparent polymers (PMMA and PI) replace the epoxy for different copper thicknesses, b) 5nm and c) 7nm.

Supporting Information 3: HSV color parameters.

Cu thickness (nm)	CI			ICI			ECI		
	H	S	V	H	S	V	H	S	V
3	70.98	2.97	90.59	51.06	12.77	91.38	57.22	5.79	97.36
4	65.66	3.61	87.34	46.15	14.58	90.95	61.31	6.61	96.18
5	53.82	4.09	84.52	40.92	18.68	92.29	54.96	9.11	97.32
6	38.34	7.56	84.78	39.14	21.10	91.30	57.40	10.32	92.17
8	58.42	3.86	78.93	36.50	25.40	95.58	38.16	19.16	94.45
10	26.07	15.46	85.25	34.98	29.02	92.60	34.70	22.91	95.26
12	31.60	13.64	81.88	34.94	30.72	94.50	34.82	23.64	94.77
14	29.72	18.75	79.93	34.07	34.75	91.17	33.02	29.97	92.70
16	29.89	20.28	78.95	34.36	36.15	89.40	33.09	31.63	91.19
18	31.02	21.95	75.52	34.26	39.74	86.66	32.97	34.19	89.03
20	31.88	24.37	72.51	33.95	41.94	84.43	32.74	36.62	85.49

Table S1. Calculated HSV (*i.e.*, Hue, Saturation, and Value) color parameters of CI, ICI, and ECI by using the experimentally measured data.

Supporting Information 4: Analytical derivation of the bending induced strain in the ITO layer of the three different structures.

A multilayer structure with the *i*th-layer (i = 1, …, N) thickness h_i, Young's modulus E_i, Poisson's ratio ν_i subjected to pure bending is depicted in Figure S3, where the origin of the y-axis locates at the top surface. According to the Euler-Bernoulli beam theory, the position of neutral axis can be found as

$$b = \frac{\sum_{i=1}^{N} \bar{E}_i \, h_i \left(\sum_{j=1}^{i} h_j - \frac{1}{2} h_i\right)}{\sum_{i=1}^{N} \bar{E}_i \, h_i} \tag{S1}$$

where $\bar{E}_i = \frac{E_i}{1-\nu_i^2}$ is the plane strain modulus of the *i*th-layer. Hence strain at $y = y_0$ can be calculated through

$$\epsilon(y_0) = \frac{b - y_0}{R} \tag{S2}$$

where R is the bending radius of the neutral axis.

The cross-sectional schematics of the thick-ITO, ICI, and ECI structures and the corresponding thickness information are provided in Figure S4. If we take $E_{\mathrm{ITO}} = 116$ GPa, $E_{\mathrm{Cu}} = 117$ GPa, $E_{\mathrm{PI}} = E_{\mathrm{SU8}} = 2.5$ Gpa and all Poisson's ratios to be 0.3, the analytical results of the maximum strain in the ITO layer of the three different strucutures subjected to different bending radii can be obtained and summarized in Table S2.

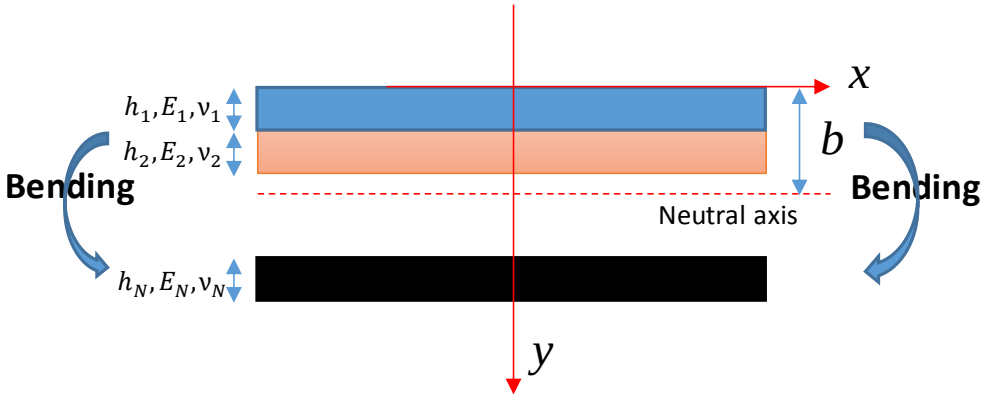

Figure S4. The schematic diagrams of multilayer neutral axis under pure bending.

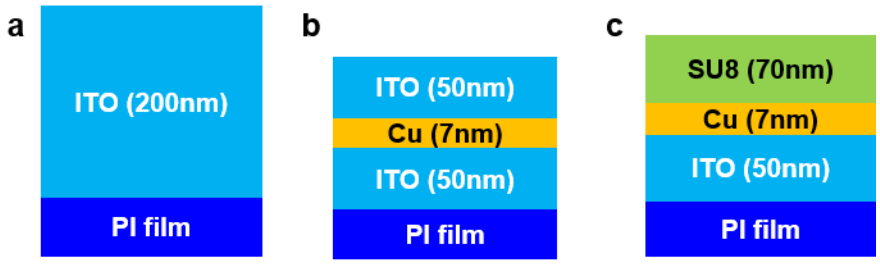

Figure S5. The cross-sectional schematic diagrams of a) thick-ITO, b) ICI, c) ECI structures.

	ITO position (y_0)	Neutral axis *b*	*R*=1.3 cm	*R*=0.52 cm	*R*=0.38 cm
Thick-ITO	0	45.92 μm	$\epsilon = 0.353\%$	$\epsilon = 0.888\%$	$\epsilon = 1.211\%$
ECI	77 nm	48.80 μm	$\epsilon = 0.375\%$	$\epsilon = 0.938\%$	$\epsilon = 1.284\%$
ICI	0	47.72 μm	$\epsilon = 0.367\%$	$\epsilon = 0.917\%$	$\epsilon = 1.256\%$

Table S2. Maximum strain of ITO in the three different structures.

Supporting Information 5: Steady state energy release rates of ITO in the three different structures.

If we neglect the very thin Cu layer in the ICI structure, both ICI and thick-ITO are essentially bilayer structures - ITO on PI. In both cases, PI substrate is much thicker than the ITO layer which is 200 nm in thick-ITO and 100 nm in ICI. The crack propagation on the surface of the film is called channel cracking as depicted in Figure S5a. The steady state energy release rate of the channel cracking is given by[1]

$$G_{\mathrm{C}} = Z_{\mathrm{c}} \frac{\sigma_0^2}{\bar{E}_{\mathrm{f}}} h \tag{S3}$$

where "C" stands for "channel", Z_{c} is a coefficient determined by the modulus mismatch between the film and the substrate $\alpha = \frac{\bar{E}_{\mathrm{f}} - \bar{E}_{\mathrm{s}}}{\bar{E}_{\mathrm{f}} + \bar{E}_{\mathrm{s}}}$ assuming they have a similar Poisson's ratio, σ_0 is the film stress, $\bar{E}_f$ is the plane strain modulus of the film, and h is the film thickness.

Since $E_f = E_{\mathrm{ITO}} = 116$ GPa, $E_s = E_{\mathrm{PI}} = E_{\mathrm{SU8}} = 2.5$ Gpa, and $\nu = 0.3$ are assumed for all materials, $\alpha = 0.95$ can be determined, which leads to $Z_c = 14$ for both the thick-ITO (TI) and ICI structures[1]. The ITO layer thickness are $h_{\mathrm{ITO}}^{\mathrm{TI}} = 200$ nm and $h_{\mathrm{ITO}}^{\mathrm{ICI}} = 100$ nm, respectively. Hence, the steady-state energy release rates of the ITO channel cracks in the thick-ITO and ICI are provided as follows:

$$G_{\mathrm{C}}^{\mathrm{TI}} = 14 \frac{\sigma_0^2}{\bar{E}_{\mathrm{f}}} h_{\mathrm{ITO}}^{\mathrm{TI}} = 56 \frac{\sigma_0^2}{\bar{E}_{\mathrm{f}}} h_0 \tag{S4}$$

and

$$G_{\mathrm{C}}^{\mathrm{ICI}} = 14 \frac{\sigma_0^2}{\bar{E}_{\mathrm{f}}} h_{\mathrm{ITO}}^{\mathrm{ICI}} = 28 \frac{\sigma_0^2}{\bar{E}_{\mathrm{f}}} h_0 \tag{S5}$$

where $h_0 = 50$ nm.

The ITO layer in the ECI is sandwiched between SU8 and PI if we neglect the very thin Cu layer in the ECI. Moreover, the crack propagation in the brittle ITO layer is referred to as tunnel cracking (Figure S5b). The steady-state energy release of the tunnel crack is presented as follows when the top and bottom layers have the same thickness and modulus[2]:

$$G_{\mathrm{T}} = \mathrm{Z}_{\mathrm{T}} \frac{\sigma_0^2}{\bar{E}_f} h \tag{S6}$$

where "T" stands for "tunnel", and Z_{T} is a coefficient determined by the mismatch of the material properties ($\alpha = \frac{\bar{E}_{\mathrm{f}} - \bar{E}_{\mathrm{s}}}{\bar{E}_{\mathrm{f}} + \bar{E}_{\mathrm{s}}}$) and the thickness ratio between the film and the substrate.

Although the PI substrate was much thicker than the top SU8 layer in the ECI structure. Eq. (S6) can still yield an upper bound of the steady-state energy release rate of the ITO

tunnel cracks in the ICI if we assume that the PI layer is as thin as the SU8 layer. Given $\alpha = 0.95$ and $h_{\mathrm{ITO}}^{\mathrm{ECI}}/h_{\mathrm{SU8}}^{\mathrm{ECI}} = 0.71$, $\mathrm{Z_T} = 0.5$ can be found[2]. Hence, the upper bound of the steady state energy release rate of the ITO tunnel cracks in ICI can be calculated as follows:

$$G_{\mathrm{T}}^{\mathrm{ECI}} = 0.5\frac{\sigma_0^2}{\bar{E}_{\mathrm{f}}}h_{\mathrm{ITO}}^{\mathrm{ECI}} = 0.5\frac{\sigma_0^2}{\bar{E}_{\mathrm{f}}}h_0 \qquad \text{(S7)}$$

Comparing the Eqs. (S4), (S5) and (S7), we found that even the upper bound of the steady-state energy release rate of the ECI ITO is still much smaller than that of the thick-ITO and ICI structures. We have also calculated the strains (or stresses) in the ITO layers of the three structures which are quite similar in SI-3. Therefore, plotting three normalized energy release rates altogether in Figure 3h provides a straightforward comparison of the crack propagation driving forces, which well explains the experimental observation that the ECI structure is the most mechanically robust one among the three different structures. The combined strain and energy release rate analyses provide us an important conclusion that the energy release rate, instead of the tensile strain, is the most reliable indicator for fracture prediction.

References

[S1] R. Huang, J. H. Prévost, Z. Y. Huang, Z. Suo, *Eng. Fract. Mech.* **2003**, 70, 2513.

[S2] S. Ho, Z. Suo, *J. Appl. Mech.* **1993**, 60, 890.

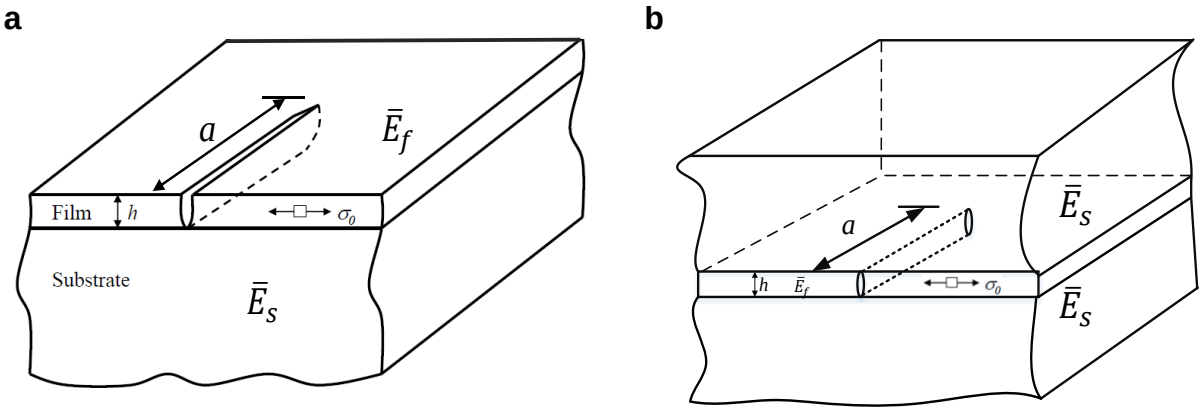

Figure S6. Schematics for a) channel crack and b) tunnel crack.

Supporting Information 6: Detailed mechanisms of force touch sensor.

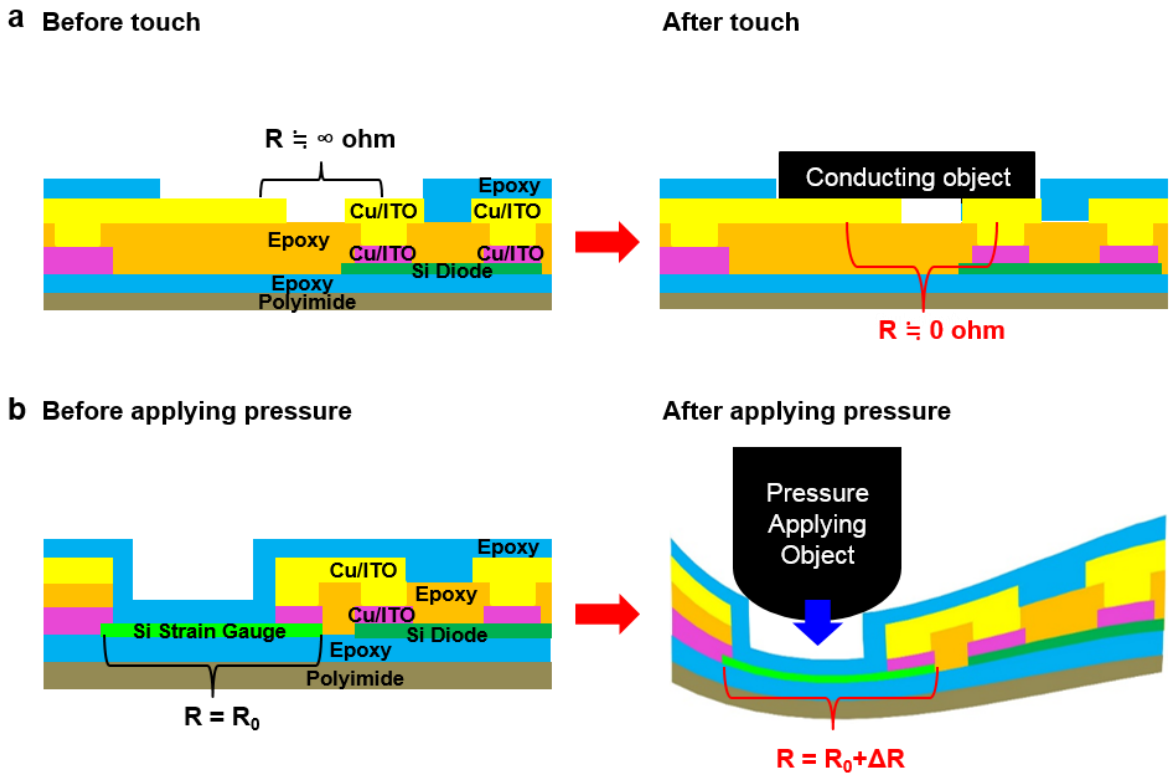

Figure S7. Detailed sensing mechanisms of the a) touch and b) pressure sensor.

Supporting Information 7: Conductive fabric on fingertips.

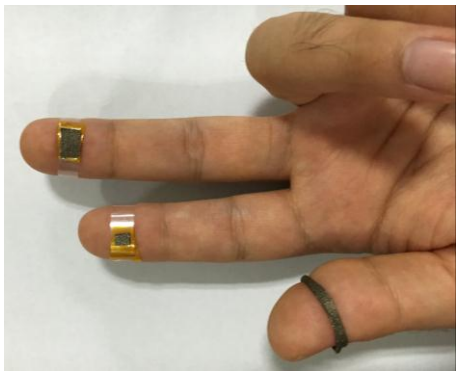

Figure S8. Photograph of the conductive fabric attached onto fingertips.

Supporting Information 8: Characterization of the touch sensor.

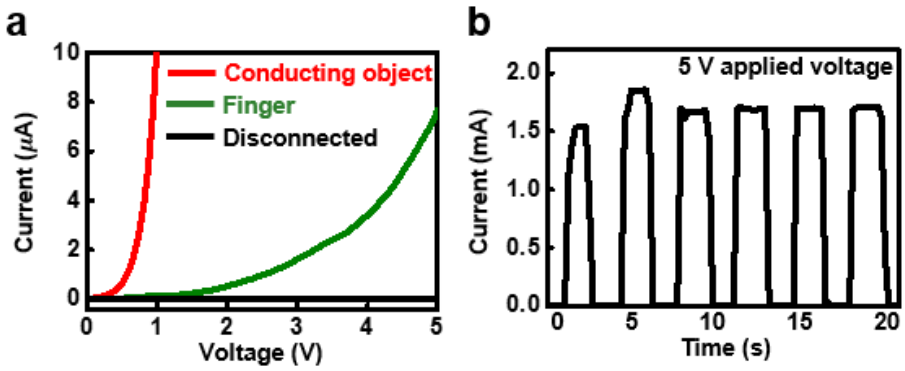

Figure S9. a) Representative *I-V* curves of the touch sensor showing the change of currents with the finger touch or the contact with a conductive fabric. b) Current change of the touch sensor showing on/off states switched using a conductive fabric.

Supporting Information 9: Real-time detection of the touched area using the touch sensor array.

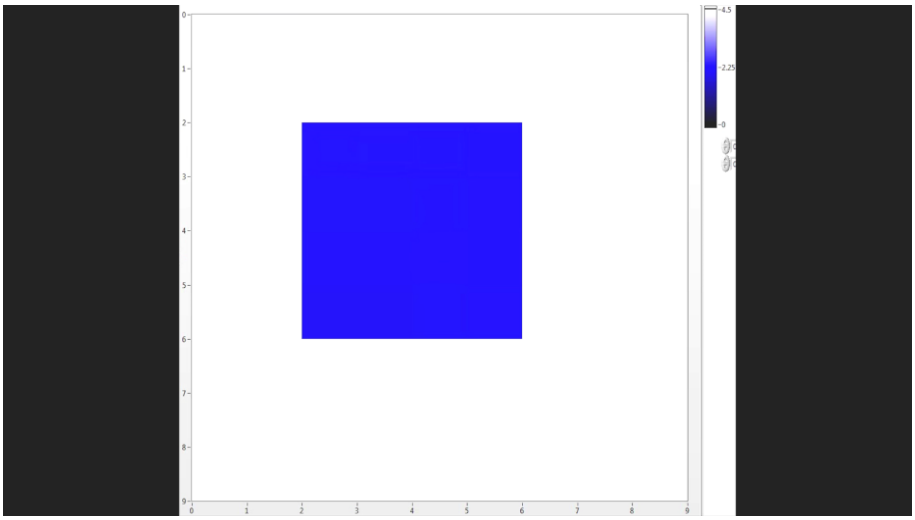

Movie S1. A movie clip showing the touched area on the touch sensor array.

Supporting Information 10: Characterization of the wearable QLEDs.

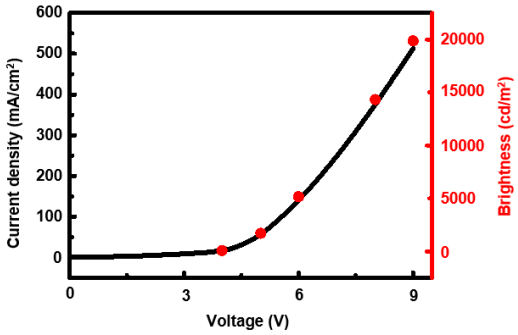

Figure S10. The *J-V-L* characteristics of the ultra-thin, wearable QLEDs.

Supporting Information 11: Characterization of the force touch sensor.

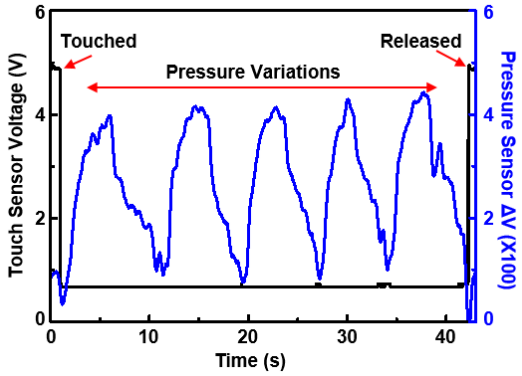

Figure S11. Plots of the output signal of the force touch sensor (both touch and pressure sensors) during varied amounts of applied pressure while remaining in contact with the touch sensor.

Supporting Information 12: LabVIEW software for the wireless drone control.

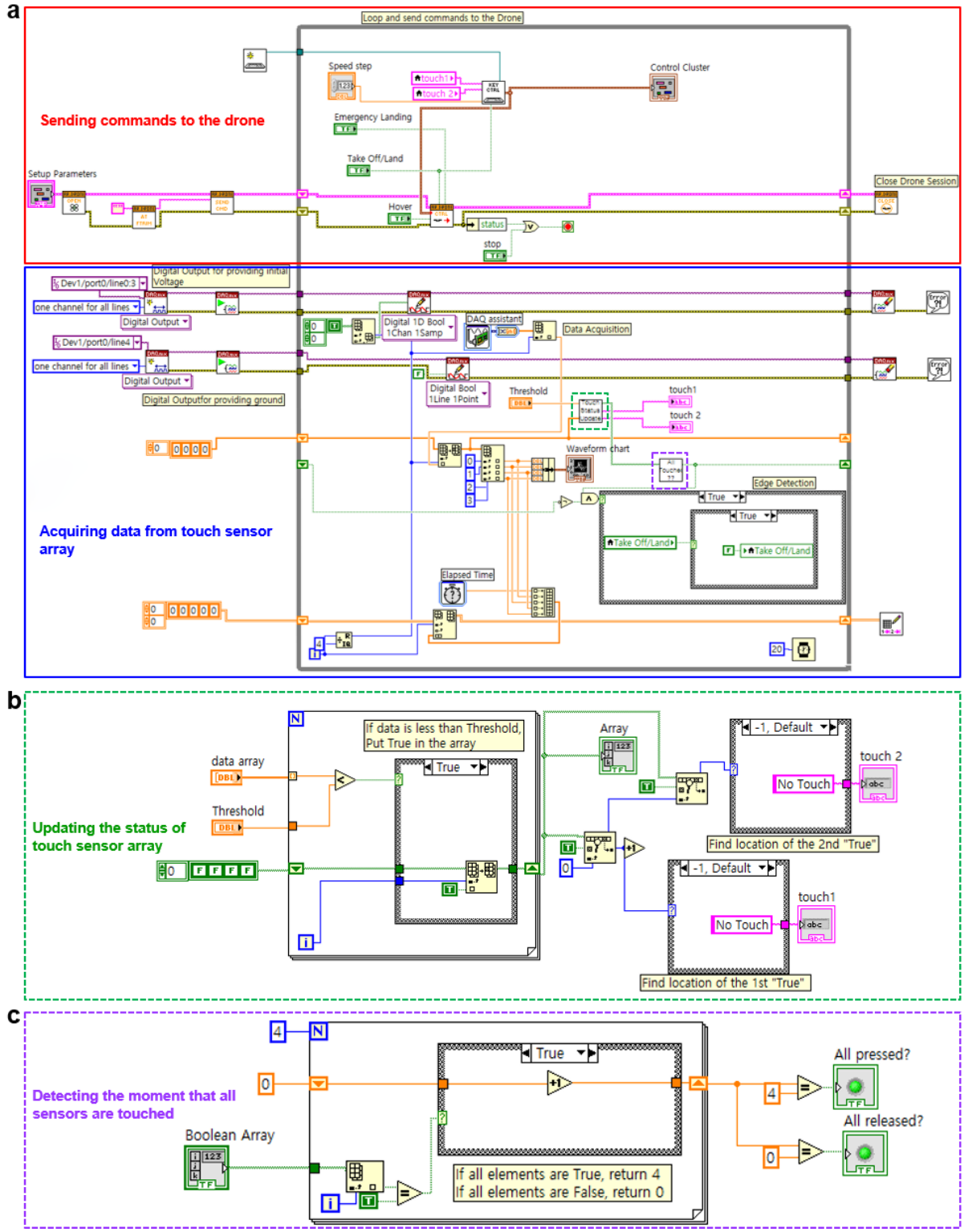

Figure S12. a) Block diagrams of the drone controlling software written by using LabVIEW. b) A sub VI for updating the status of the touch sensor array, indicated as the greed dotted box in a). c) A sub VI for detecting the moment that all sensors are touched, indicated as the purple dotted box in a).

Supporting Information 13: Confusion matrix.

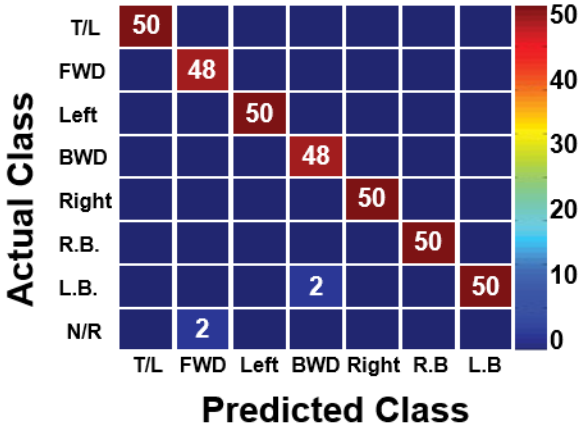

Figure S13. Confusion matrix that describes the accuracy in classification of the commands. T/L: Taking off/Landing, R.B: Right backward, L.B: Left backward, N/R: No response.

Supporting Information 14: Drone control movie.

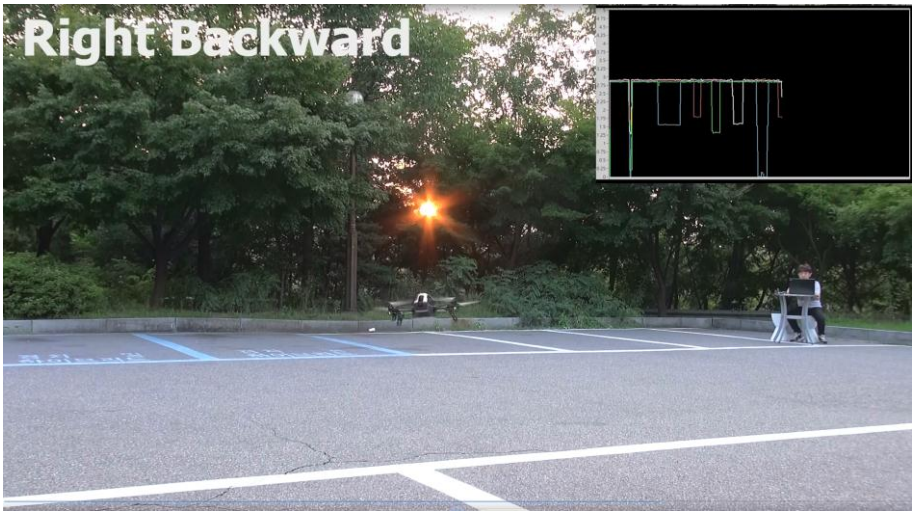

Movie S2. A movie clip that demonstrates wireless drone control using the force touch sensor array.